



Dislocation Loops in Proton Irradiated Uranium-Nitrogen-Oxygen System

December 2021

Changing the World's Energy Future

Pengyuan Xiu, Miaomiao Jin, Kaustubh Krishna Bawane, Beata Tyburska-Pschel, Brian J. Jaques, Kevin G. Field, Jeffrey J Giglio, Lingfeng He



INL is a U.S. Department of Energy National Laboratory operated by Battelle Energy Alliance, LLC

DISCLAIMER

This information was prepared as an account of work sponsored by an agency of the U.S. Government. Neither the U.S. Government nor any agency thereof, nor any of their employees, makes any warranty, expressed or implied, or assumes any legal liability or responsibility for the accuracy, completeness, or usefulness, of any information, apparatus, product, or process disclosed, or represents that its use would not infringe privately owned rights. References herein to any specific commercial product, process, or service by trade name, trade mark, manufacturer, or otherwise, does not necessarily constitute or imply its endorsement, recommendation, or favoring by the U.S. Government or any agency thereof. The views and opinions of authors expressed herein do not necessarily state or reflect those of the U.S. Government or any agency thereof.

Dislocation Loops in Proton Irradiated Uranium-Nitrogen-Oxygen System

Pengyuan Xiu, Miaomiao Jin, Kaustubh Krishna Bawane, Beata Tyburska-Pschel, Brian J. Jaques, Kevin G. Field, Jeffrey J Giglio, Lingfeng He

December 2021

**Idaho National Laboratory
Idaho Falls, Idaho 83415**

<http://www.inl.gov>

**Prepared for the
U.S. Department of Energy
Under DOE Idaho Operations Office
Contract DE-AC07-05ID14517**

Pengyuan Xiu^{a,b*}, Miaomiao Jin^c, Kaustubh Bawane^a, Beata Tyburska-Püschel^d, Brian J. Jaques^c, Kevin G. Field^b, Jeffrey J. Giglio^a, Lingfeng He^{a*}

^a Idaho National Laboratory, Idaho Falls, ID 83415, USA

^b Department of Nuclear Engineering and Radiological Sciences, University of Michigan, Ann Arbor, MI 48109, USA

^c Department of Nuclear Engineering, The Pennsylvania State University, University Park, PA 16802, USA

^d Dutch Institute for Fundamental Energy Research, 5612 AJ Eindhoven, The Netherlands

^e Micron School of Materials Science and Engineering, Boise State University, Boise, ID 83725, USA

Abstract

In this study, we investigated the dislocation loop types formed in the proton-irradiated uranium-nitrogen-oxygen (U-N-O) system, which involves uranium mononitride (UN), uranium sesquinitride (α -U₂N₃), and uranium dioxide (UO₂) phases. The dislocation loop formation is examined using specimens irradiated at 400°C and 710°C. Based on the detailed transmission-based electron microscopy characterization with i) the morphology-based on-zone and ii) the invisibility-criterion based two-beam condition imaging techniques, only a single type of dislocation loop in each phase is found: $a/2\langle 110 \rangle$, $a/2\langle 111 \rangle$, or $a/3\langle 111 \rangle$ dislocation loops in UN, α -U₂N₃, and UO₂ phases, respectively. Molecular statics calculations for the formation energy of perfect and faulted dislocation loops in the UN phase indicate a critical loop size of ~ 6 nm, above which perfect loops are thermodynamically favorable. This could explain the absence of faulted loops in the experimental observation of the irradiated UN phase at two temperatures. This work will enhance the understanding of irradiation induced microstructural evolution for uranium mononitride as advanced nuclear fuels for the next-generation nuclear reactors.

Keywords: radiation effects; dislocation loops; uranium nitride; nuclear fuels

*Corresponding authors: Pengyuan Xiu, xiupy@umich.edu

Lingfeng He, lingfeng.he@inl.gov

1. Introduction

Uranium mononitride (UN) has been considered a candidate fuel material for advanced nuclear systems including liquid metal-cooled fast reactors, high-temperature gas-cooled reactors, and light water reactors (LWRs) [1–10] due to its multiple advantages [3]: (i) higher fissile density (40% more uranium in UN than in uranium dioxide, UO_2), (ii) higher thermal conductivity, (iii) easier preprocessing, (iv) good irradiation stability and chemical compatibility with most potential cladding materials, and (v) longer fuel cycle time. The oxidation and corrosion of UN in LWRs [11–15], however, is the major challenge for its wide-spread adoption as a nuclear fuel. Moreover, the formation of new phases after oxidation results in additional complexities for (i) material property examinations, such as microstructural evolution, radiation resistance and thermal conductivity, as well as (ii) modeling of UN fuel performance.

Under irradiation, the formation of dislocation loops is known to decrease thermal conductivities of nuclear fuels because of phonon defect scattering [16]. Therefore, it is important to conduct detailed characterization of dislocation loops in irradiated fuels. Recently, the phase and dislocation loop evolution in the uranium-nitrogen-oxygen system under proton irradiation was studied [9]. Irradiation can enhance the oxidation of UN, which leads to the formation of two phases that are fully coherent, alpha uranium sesquinitride ($\alpha\text{-U}_2\text{N}_3$) and UO_2 [9]. UN has a rocksalt crystal structure, $\alpha\text{-U}_2\text{N}_3$ has a body-center-cubic (BCC) based Mn_2O_3 -type crystal structure [17], and UO_2 has a fluorite crystal structure [18]. The dislocation loop size was found three times larger in the two nitride phases, UN and $\alpha\text{-U}_2\text{N}_3$, than in UO_2 , while the number density was one order of magnitude higher in UO_2 than in the nitride phases [9].

Besides dislocation loop size and density, the characteristics of dislocation loops, however, such as the Burgers vector and habit plane in the abovementioned three phases under proton

irradiation have not been studied in detail. Although the defects in actinide nitrides are rarely investigated, zirconium nitride (ZrN) was used as a common non-radioactive surrogate for UN to study the radiation effects [19,20] because ZrN shares the same crystal structure with UN. Yang et al. [19] used the high-resolution transmission electron microscopy (HRTEM) technique to show that vacancy-type pyramidal dislocation loops formed in ZrN under proton irradiation to 0.75 dpa at 800°C, whereas faulted dislocation loops were not observed using rel-rod dark field imaging technique. Bao et al. [21] showed $a/2\langle 110 \rangle$ dislocation loop formation in the polycrystalline ZrN under gold irradiation. In another study, Jiao et al. [20] observed both interstitial- and vacancy-types of dislocation loops using HRTEM in iron irradiated nanocrystalline ZrN films.

Dislocation loop analysis in the traditional nuclear fuel, UO_2 , under heavy ion irradiation (using Cs, Kr, or Xe ions) has been studied for decades. These studies [22–25] showed the exclusive existence of $a/2\langle 110 \rangle$ perfect type of dislocation loops in heavy ion irradiated UO_2 , whereas very limited neutron or electron irradiation experimental data [26] showed the existence of only $a/3\langle 111 \rangle$ faulted dislocation loops. Additionally, molecular dynamics (MD) simulation studies of UO_2 [27–29] indicated that interstitial clusters may initially aggregate to form small $a/3\langle 111 \rangle$ faulted dislocation loops, which is a more stable configuration compared to $a/2\langle 110 \rangle$ perfect dislocation loops. With increasing size, unfaulting can occur because of the increasing stacking fault energy, which has been reported by experiments and simulations in irradiated face-center-cubic (FCC) materials [30–38]. Besides the direct investigation of irradiated UO_2 , dislocation loop analysis of ion irradiated thorium dioxide (ThO_2), sharing the same crystal structure of UO_2 , has also been studied. Mixed data have been reported [39–41] in irradiated ThO_2 with the formation of $a/2\langle 110 \rangle$ and/or $a/3\langle 111 \rangle$ type of dislocation loops due to different irradiation conditions such as ion species, temperatures, and damage levels.

To analyze proton-irradiation-induced dislocation loops in the U-N-O system (three phases: UN and α -U₂N₃, and UO₂), we used developed scanning/transmission electron microscopy (S/TEM) techniques with the aid of several methods for classification of loop types based on observed contrast and morphology [42–44]. The on-zone STEM technique coupled with simulated morphology maps has been recently developed and applied to characterize dislocation loop formation in irradiated FCC [44] and BCC [42,43] alloys. It has been demonstrated that dislocation loops of various types [35,44–47] in these alloys can be unambiguously identified, given the correct orientation being used, based on their projection morphology when the dislocation loop size is above a given size threshold, typically around 5-10 nm for most STEM instruments and imaging conditions. In addition, STEM imaging has multiple advantages of (i) suppressing background contrast to improve signal-to-noise ratio [48], (ii) exhibiting all dislocation loops within the TEM specimen when the on-zone condition is satisfied [49], and (iii) the applicability of some common conventional transmission electron microscopy (CTEM) techniques for dislocation loop analysis such as the two-beam condition imaging that utilizes the $\vec{g} \cdot \vec{b}$ invisibility criterion [50,51]. Furthermore, to gain a fundamental understanding towards the observed dislocation loop types, MD simulations are applied to reveal the energetically favorable atomic configuration and calculate the size-dependent formation energy of dislocation loops in irradiated UN.

2. Methods

2.1 Proton Irradiation

The fabrication and the initial microstructures of the UN-5wt.%UO₂ sample was provided in a previous study [9,14]. The bulk sample was irradiated with 2 MeV proton ions to reach the total fluence of 8×10^{18} ions/cm² at 400°C and 710°C, respectively [9]. Proton irradiation was chosen in

this study, because (i) it has been successfully used to separate the effects of specific defects on thermal conductivity of oxide fuels [16], and (ii) it creates a relatively flat damage region over tens of μm by a few MeV energy, which is good for modern thermal transport measurements [16,52]. The proton flux was maintained at 5.2×10^{13} ions/(cm^2s) for the low-temperature irradiation and 7.5×10^{13} ions/(cm^2s) for the high-temperature irradiation, resulting in a damage rate of 4.1×10^{-6} and 5.9×10^{-6} dpa/s, respectively for UN. The Stopping and Range of Ions in Matter (SRIM) 2013 code in “Detailed Calculation with Full Damage Cascades” mode [53] was used to calculate the proton-irradiation damage with the damage profiles for UN, $\alpha\text{-U}_2\text{N}_3$ and UO_2 shown previously [9]. The region of interest of below 3 μm is located at the common plateau portion of the damage curves of three phases, where the damage dose is about 0.5~0.6 dpa for the three phases. Based on the SRIM results, the calculated dose varied by only 10% across the three phases, which is within the variance expected for a single phase across the depth region investigated. This depth range was selected with the purpose of avoiding significant injected-proton-interstitial effects [54,55].

2.2 Microstructural Characterization

After the ion irradiation, the “lift-out” technique using focused ion beam (FIB) equipped on an FEI Quanta 3D scanning electron microscope was conducted to prepare electron-transparent specimens, followed by low-energy (5 kV and 2 kV) ion sputtering to reduce FIB-induced damages on the sample surface. Three phases, UN, $\alpha\text{-U}_2\text{N}_3$, and UO_2 after irradiation at two temperatures, were identified and located by performing energy-dispersive X-ray spectroscopy (EDS) mapping using a Titan Themis 200 Scanning and Transmission Electron Microscope (S/TEM). Detailed chemical mapping results with limited strain-based contrast imaging have been reported in the previous study [9].

Dislocation loop characterization and Burgers vector analysis for the two nitride-based phases were conducted with two techniques: (i) two-beam condition imaging in STEM mode using the $\vec{g} \cdot \vec{b}$ invisibility criterion [56] involving multiple tilting conditions, and (ii) the recently developed on-zone STEM imaging [42–44]. Note that only the *family* of dislocation loops were determined, i.e., Burgers vectors, whereas the *nature* of dislocation loops is not within the scope of this study. The diffraction patterns were obtained after the sample tilting using CTEM, and then STEM was used for imaging at the selected tilting conditions. The zone axes used for all the dislocation loop characterization were one of the commonly used major low-index ones including [001], [011], and [111] because the dislocation loop morphology maps are available in the literature for the FCC (similar to UN) and BCC (similar to α -U₂N₃) crystal structures, and the \vec{g} vectors near these zone axes were selected to be low-order as well.

Dislocation loop characterization in proton irradiated UO₂ at 710°C was conducted using the $\vec{g} \cdot \vec{b}$ invisibility criterion in CTEM mode. The characterization for UO₂ irradiated at 400°C was not conducted because dislocation loops are too small (e.g., < 5 nm) to be identified using S/TEM techniques, especially with the existence of possible FIB-induced black-dot damage.

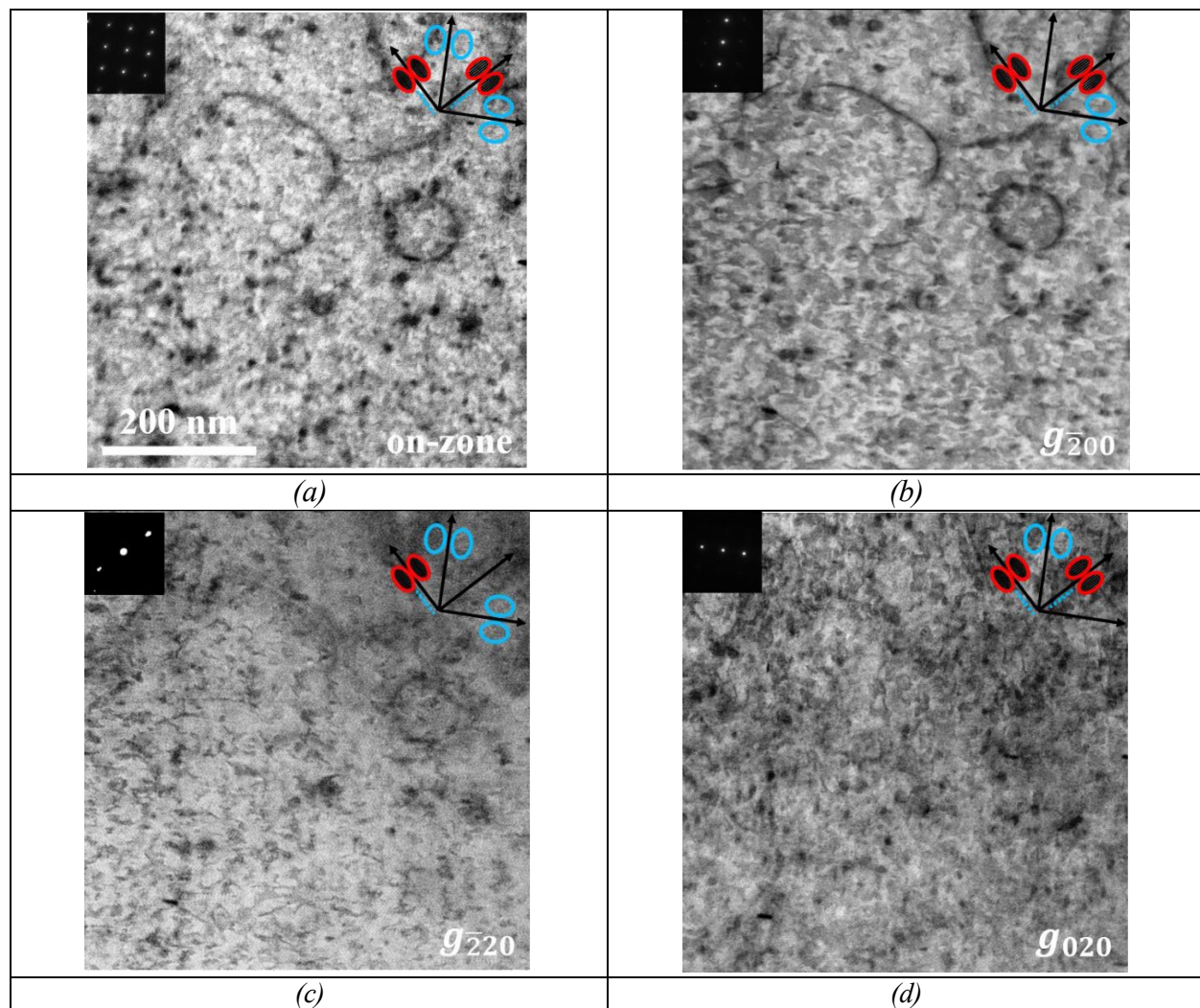
3. Results

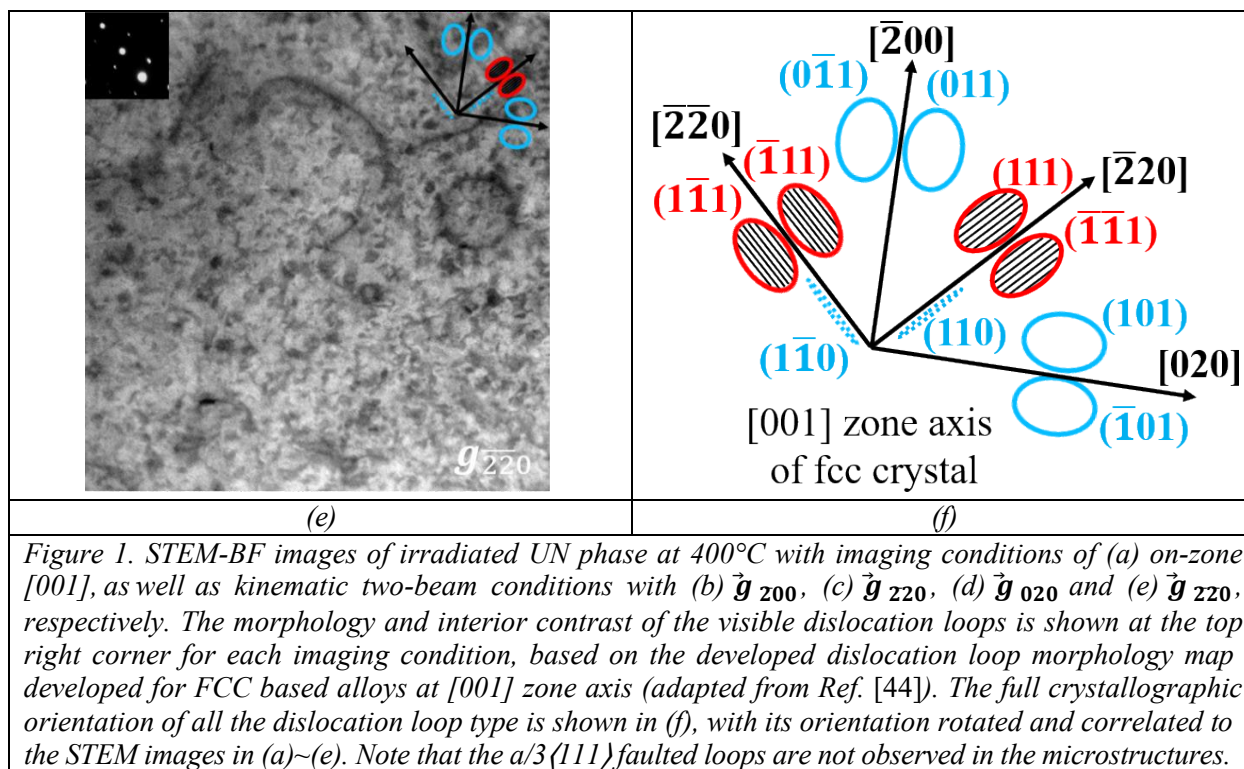
3.1 Dislocation Loops in UN after Irradiation at 400°C and 710°C

Figure 1 shows the dislocation loop structures in the UN phase after irradiation at 400°C. The on-zone [001] STEM bright-field (STEM-BF) image exhibits all dislocations and dislocation loops, while kinematic two-beam condition STEM-BF images utilizing $\vec{g} \cdot \vec{b}$ invisibility criterion reduce or eliminate the contrast of some of the dislocation loops. Multiple \vec{g} conditions are sequentially achieved near the [001] zone axis, including \vec{g}_{200} , \vec{g}_{201} , \vec{g}_{020} and \vec{g}_{210} . The dislocation loop

114 morphology map developed for irradiated FCC-based alloys at $[001]$ zone axis (adapted from Ref.
 115 $[44]$) is shown in Figure 1 as well. Because the rocksalt crystal structure of UN is similar to the
 116 FCC crystal structure, similar types of dislocation loops, i.e., $a/2\langle 110 \rangle\{110\}$ perfect and
 117 $a/3\langle 111 \rangle\{111\}$ faulted loops, if exist, are expected to form under irradiation.

118



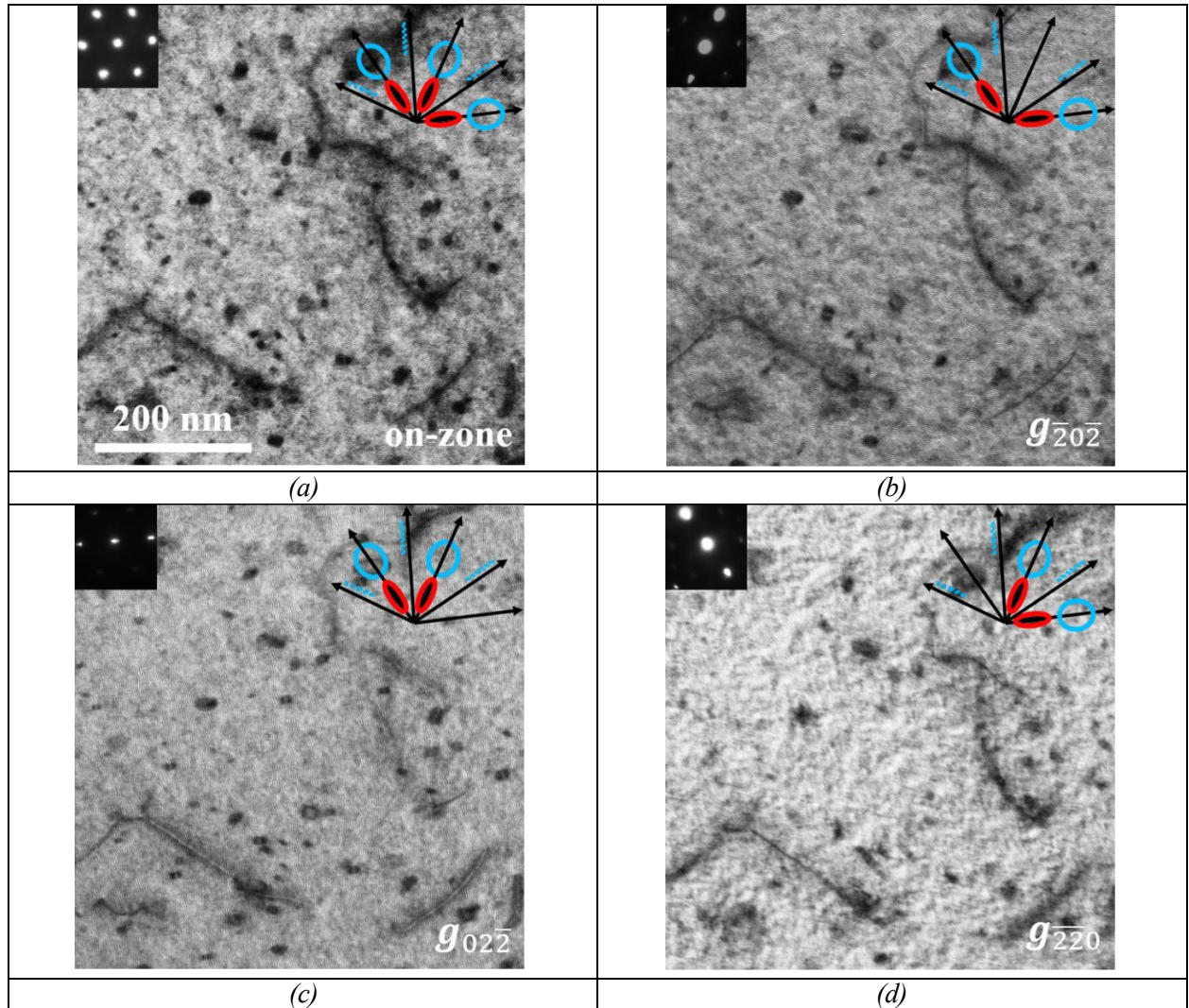


As can be seen, there is no $a/3\langle 111 \rangle$ faulted dislocation loop observed in irradiated UN at the temperature of 400°C, because (i) the interference shadow contrast would have been exhibited if faulted loops exist in irradiated or quenched FCC alloys [32,35,44,57–59] due to the inserted faulted plane causing a phase change of the electron wave [56,60], and (ii) no loops appear or disappear in the same way as the faulted dislocation loops in the STEM images of different two-beam conditions that is determined by the $\vec{g} \cdot \vec{b}$ invisibility criterion. Therefore, all observed dislocation loops are considered to be perfect-type in the irradiated UN, assuming all faulted loops would appear non-edge-on at the $[001]$ viewing direction.

The irradiation-induced dislocation loop structures at 710°C are shown in Figure 2, with the on-zone $[\bar{1}11]$ STEM-BF image exhibits all dislocations and dislocation loops, as well as three kinematic two-beam condition STEM-BF images near the $[\bar{1}11]$ zone axis with \vec{g}_{202} , \vec{g}_{022} and

\vec{g}_{220} , respectively. The dislocation loop morphology map developed for irradiated FCC-based alloys at $[\bar{1}11]$ zone axis (adapted from Ref. [44]) is shown in Figure 2 as well. Again, only the perfect dislocation loops in the microstructure exist after the proton irradiation at 710°C.

Note that Moiré fringes are observed in the UN phase irradiated at both 400°C and 710°C, as shown in Figures 1 and 2. They are likely a result of the new phases formed from the surface oxidation after the TEM sample preparation, due to the susceptibility to oxidation of the UN phase at the room temperature [9].



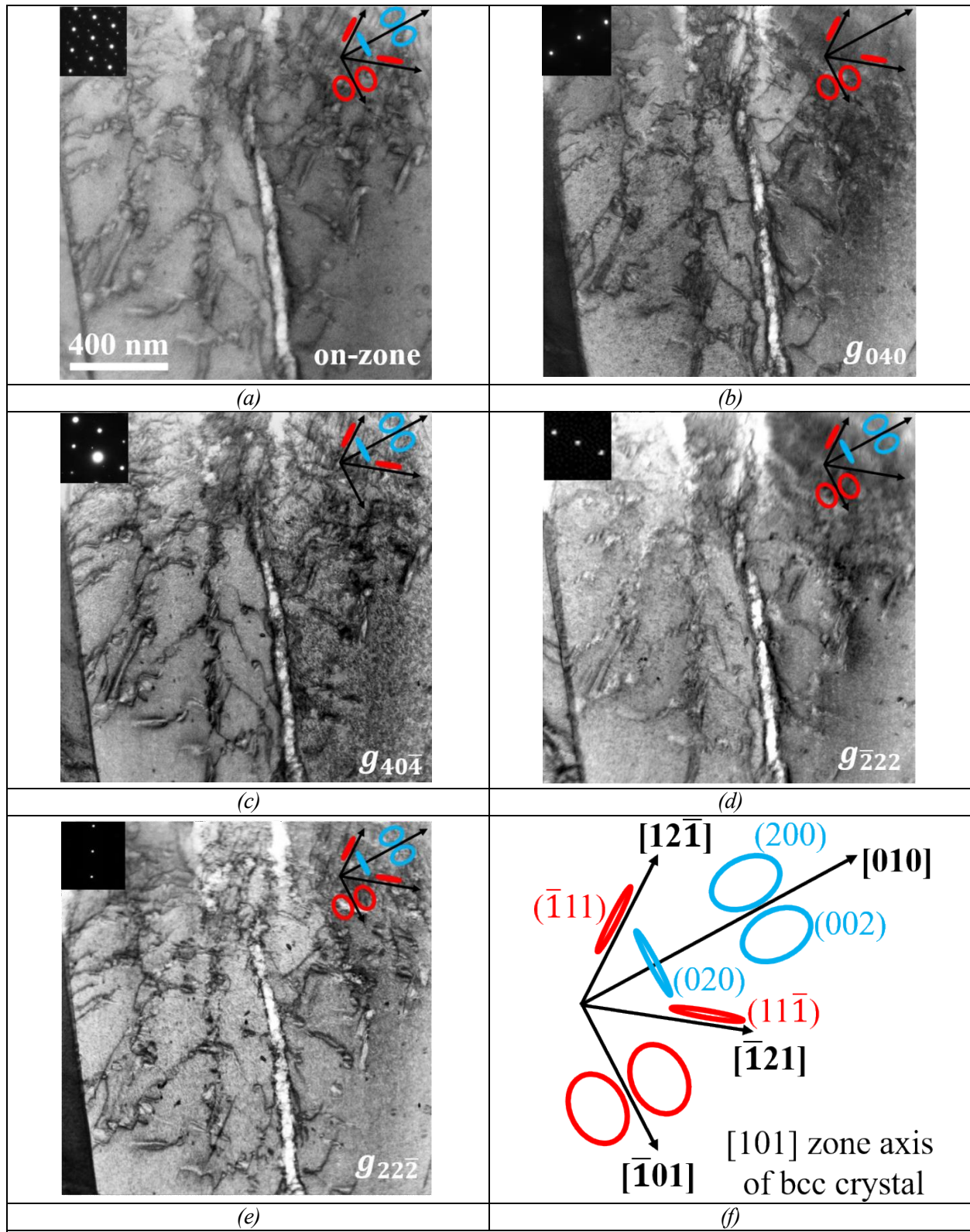


Figure 3. STEM-BF images of irradiated α - U_2N_3 phase at 400°C with imaging conditions of (a) on-zone $[101]$, as well as kinematic two-beam conditions with (b) \vec{g}_{040} , (c) \vec{g}_{404} , (d) \vec{g}_{222} and (e) \vec{g}_{222} , respectively. The morphology of the visible dislocation loops is shown at the top right corner for each imaging condition, based on the developed dislocation loop morphology map developed for BCC based

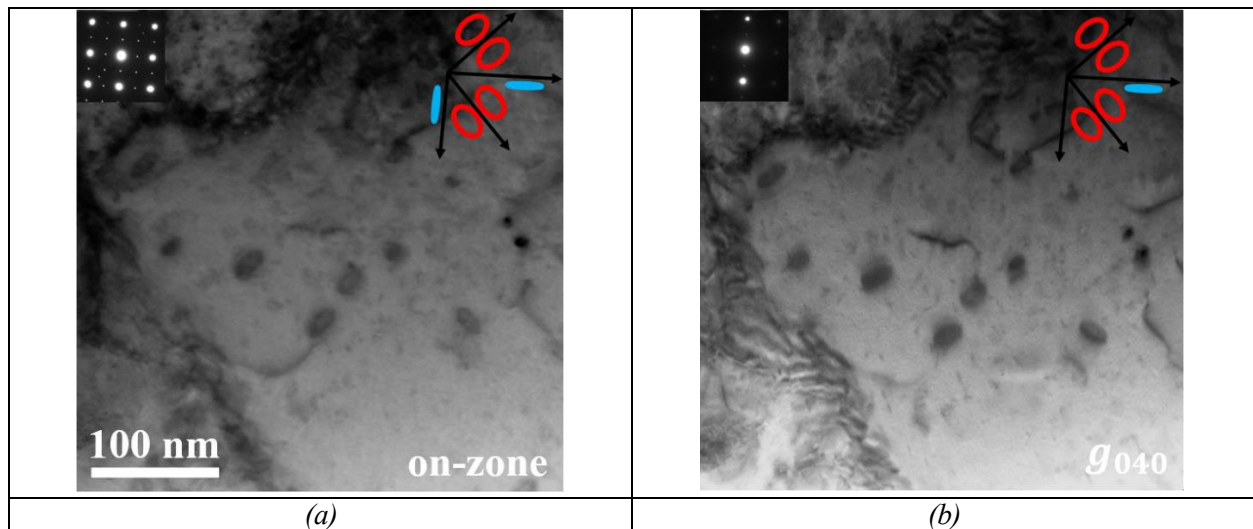
alloys at $[101]$ zone axis (adapted from Ref. [42]). The full crystallographic orientation of all the dislocation loop type is shown in (f), with its orientation rotated and correlated to the STEM images in (a)~(e). Note that the $a\langle 100 \rangle$ loops are not observed in the microstructures.

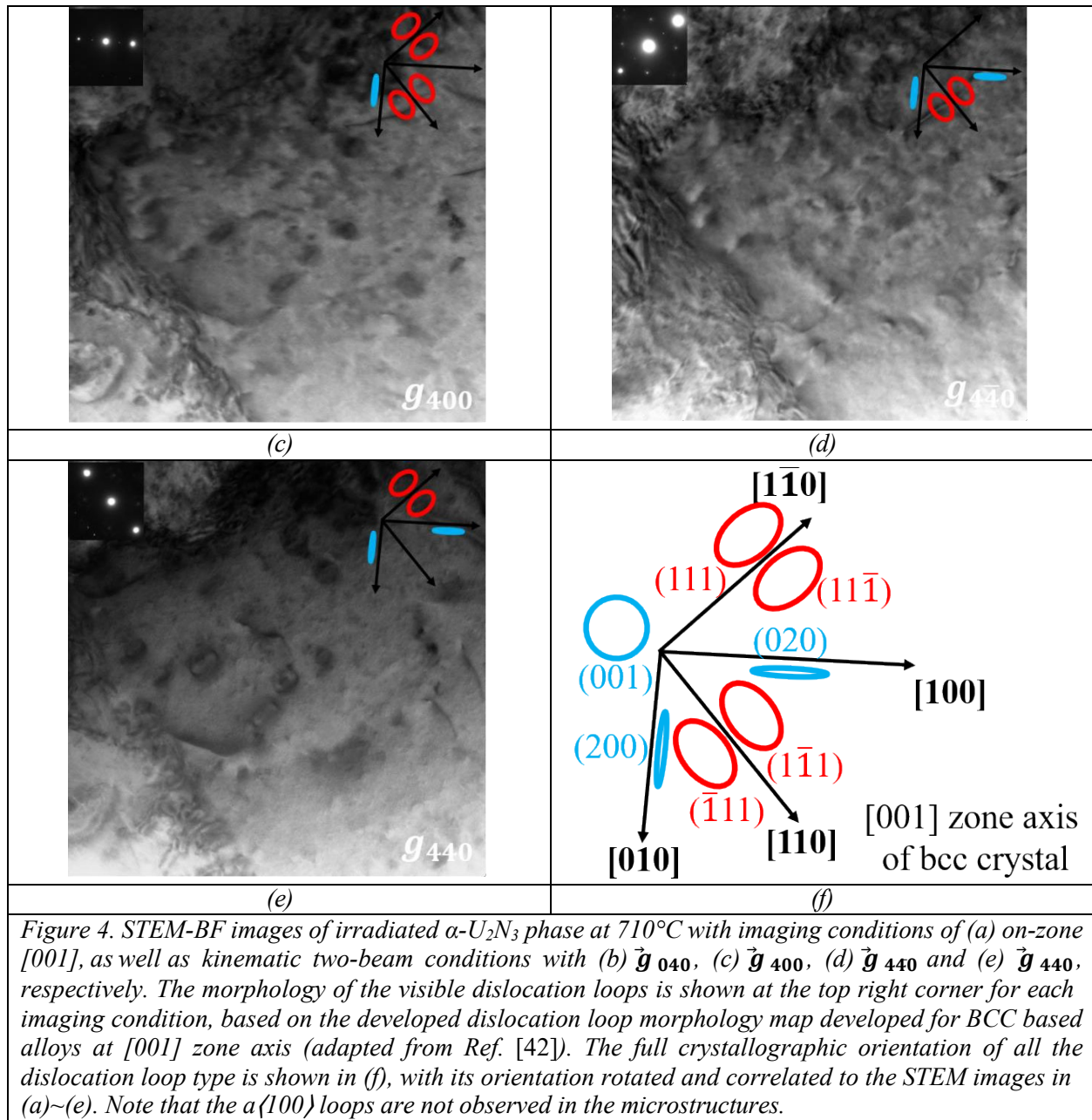
148

149 By carefully examining the visibility of dislocation loops under all the selected two-beam
150 conditions, as well as their morphology prediction, it is determined that only $a/2\langle 111 \rangle$ type of
151 dislocation loops exist in the irradiated $\alpha\text{-U}_2\text{N}_3$ at 400°C , while a $\langle 100 \rangle$ loops are not observed.

152 In addition, all the dislocations are also identified with the type of $a/2\langle 111 \rangle$.

153 At a higher temperature of 710°C , the proton irradiation-induced dislocation loop structures
154 are shown in Figure 4 in corresponding STEM images. In this case, again, only the $a/2\langle 111 \rangle$ type
155 dislocation loops are identified from the elliptical shape and the direction of the major axis
156 observed, and by the comparison with the dislocation loop morphology map in Figure 4(f). Note
157 that the weak double diffraction spots are observed and might result from ordered oxygen atoms
158 present in the $\alpha\text{-U}_2\text{N}_3$ lattice [61].





159

160 3.3 Dislocation Loops in UO_2 after Irradiation at 710°C

161 The dislocation loop structures of proton irradiated UO_2 at 710°C are shown in Figure 5, with
 162 the Burgers vector analysis conducted by using the $\vec{g} \cdot \vec{b}$ invisibility criterion in the CTEM mode.
 163 This technique was chosen for loop type analysis in irradiated UO_2 over the previously mentioned

morphology-based technique, because as can be seen in Figure 5, the dislocation loop size is quite small (< 5 nm), making the morphology ambiguous to identify.

Figure 5 shows CTEM-BF images of UO_2 phase obtained using various g conditions near $[001]$ zone axis, including \vec{g}_{200} , \vec{g}_{220} and $\vec{g}_{2\bar{2}0}$. Table 1 shows invisibility criteria for dislocation loops with four variants of $a/3\langle 111 \rangle$ faulted type and six variants of $a/2\langle 110 \rangle$ perfect type Burgers vector directions under the three selected \vec{g} two-beam conditions. In Figure 5, two different families of dislocation loops were identified by letters A and B and colors red and yellow, respectively. Family A dislocation loops were visible at \vec{g}_{200} and \vec{g}_{220} , while became invisible at $\vec{g}_{2\bar{2}0}$ as shown in Figure 5(a), 5(b) and 5(c), respectively. Family B dislocation loops were visible at \vec{g}_{200} and $\vec{g}_{2\bar{2}0}$ while disappears at \vec{g}_{220} as shown in Figure 5(a), 5(b) and 5(c), respectively. Table 1 also lists possible Burgers vector directions for loop family A and B based on their appearances and disappearances at given \vec{g} conditions. Burgers vector direction of loop family A was either $[111]$ or $[\bar{1}\bar{1}1]$ or $[110]$, while Burgers vector direction of loop family B was either $[1\bar{1}\bar{1}]$ or $[1\bar{1}1]$ or $[\bar{1}10]$, as shown in Table 1. It should be noted that current \vec{g} conditions identify both loop families A and B as either $a/3\langle 111 \rangle$ type faulted dislocation loops or $a/2\langle 110 \rangle$ type perfect dislocation loops.

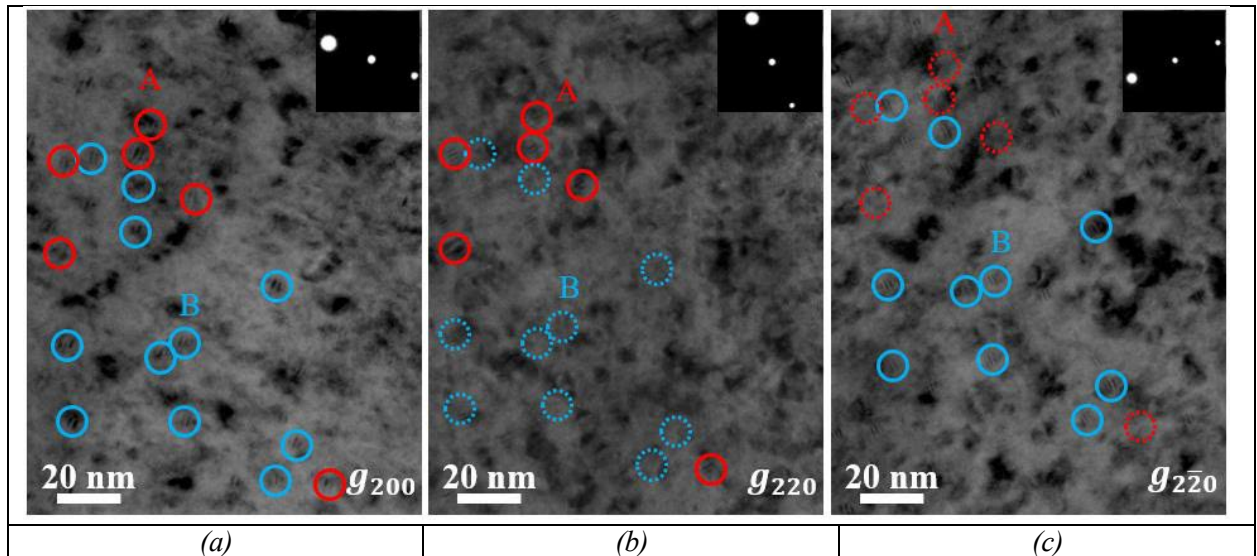






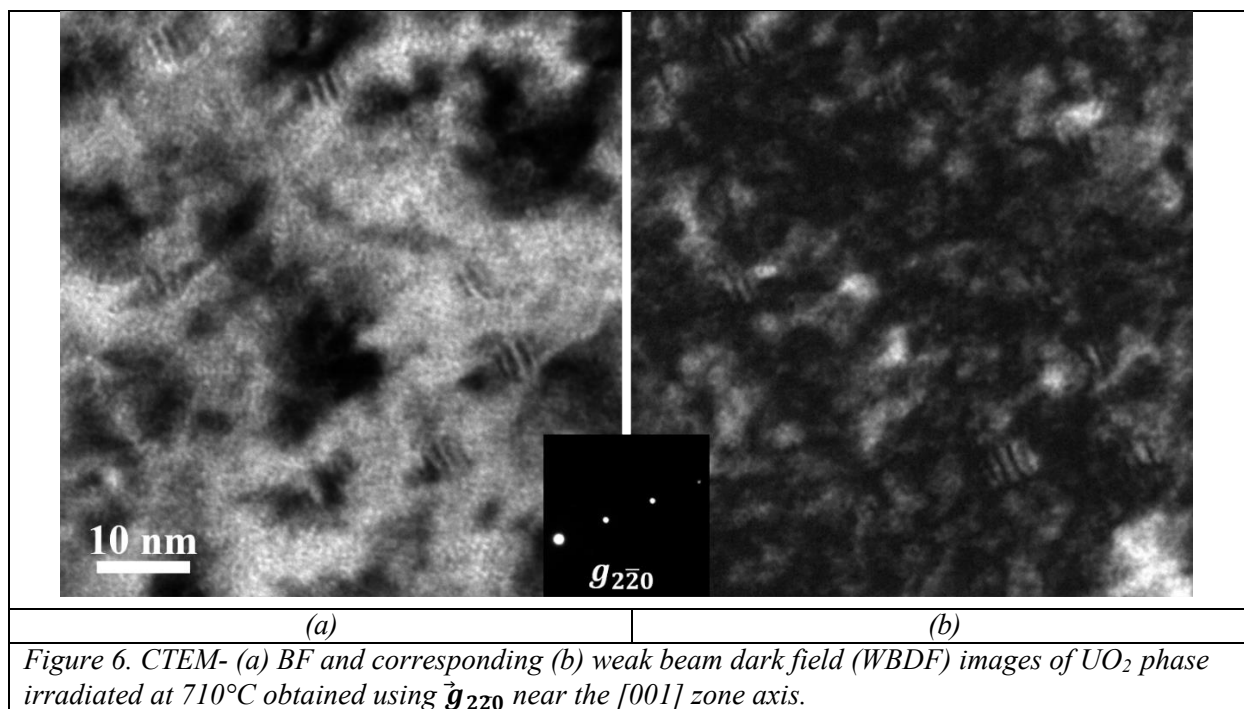


Figure 5. CTEM-BF images of irradiated UO₂ phase at 710°C with imaging conditions of kinematic two-beam conditions with (a) \vec{g}_{200} , (b) \vec{g}_{220} , and (c) $\vec{g}_{2\bar{2}0}$ near the [001] zone axis. Note that the dislocation loop size in the irradiated UO₂ phase is so small that the morphology-based technique mentioned before may not readily apply due to the ambiguous observed dislocation loop morphology.

Table 1. Burgers vector analysis using $\vec{g} \cdot \vec{b} = 0$ invisibility criterion for the proton irradiated UO₂ phase at 710°C. “V” and “I” denote dislocation loops being “visible” or “invisible”, respectively, under certain \vec{g} conditions.

b	\vec{g} (zone axis = [001])			Identified loops
	[200]	[220]	[2 $\bar{2}$ 0]	
a/3[111]	V	V	I	A 
a/3[$\bar{1}\bar{1}\bar{1}$]	V	V	I	A 
a/3[1 $\bar{1}\bar{1}$]	V	I	V	B 
a/3[1 $\bar{1}$ 1]	V	I	V	B 
a/2[011]	I	V	V	–
a/2[101]	V	V	V	–
a/2[110]	V	V	I	A 
a/2[0 $\bar{1}\bar{1}$]	I	V	V	–
a/2[1 $\bar{0}\bar{1}$]	V	V	V	–
a/2[$\bar{1}\bar{1}$ 0]	V	I	V	B 

To further confirm the dislocation loop type, high magnification CTEM-BF and weak beam dark field (WBDF) images of dislocation loops using the (g, 2g) condition in the irradiated UO₂ phase at $g = [2\bar{2}0]$ near [001] zone axis are shown in Figure 6(a) and 6(b), respectively. It is seen that dislocation loops have elliptical shape with stacking fault fringes inside of it. Since only faulted a/3<111> type dislocation loops can contribute the inserted extra plane that causes faulted stacking sequence, it can be concluded that loop family A and loop family B are both of different variants, but both are a/3<111> type faulted dislocation loops. This observation is in good agreement with the proton irradiation ThO₂ in the previous study [40], where only a/3<111> type of faulted dislocation loops were found.



4. Discussion

To examine the structure and energetics of the two types of dislocation loops in UN, we applied molecular statics (MS) calculation using the LAMMPS package (<https://lammps.sandia.gov>) [62]. The interatomic potential considering the angular dependence was developed by Tseplyaev and Starikov [63], based on force-matching to DFT database. This potential was demonstrated to have a low fitting error and well-reproduced thermodynamic properties for the B1-phase of UN [63]. Therefore, this potential is utilized. Note that it does not explicitly consider charge property, which may be justified by the fact that the bonding between U and N atoms is metallic-like [64].

In the crystal structure of B1-phase, there are predominantly two types of dislocation loops formed under irradiation, i.e. $a/3\langle 111 \rangle$ faulted loops and $a/2\langle 110 \rangle$ perfect loops. Notably, the faulted loops have been reported in irradiated titanium carbide (TiC) [65,66], zirconium carbide (ZrC) [67] and high-entropy carbide [68]. Here, we consider pure-edge type $a/3\langle 111 \rangle$ and $a/2\langle 110 \rangle$

207 loops on $\{111\}$ and $\{110\}$ habit planes, respectively. To ease the construction of loops, perfect
208 simulation cells with z-axis oriented in $[111]$ ($15.2 \text{ nm} \times 15.5 \text{ nm} \times 10.1 \text{ nm}$, 164,736 atoms) and
209 $[011]$ directions ($15.6 \text{ nm} \times 15.2 \text{ nm} \times 10.3 \text{ nm}$, 168,960 atoms) are created and relaxed to ground
210 state, respectively.

211 To study the energetics of perfect and faulted dislocation loops in UN, we need to first identify
212 the atomic structure for the loops. For $a/3\langle 111 \rangle$ loop, due to the electrostatic interaction, a single
213 layer of $\{111\}$ loop would be energetically prohibited. With double layer $\{111\}$ loops, the
214 stoichiometry can significantly reduce the energy penalty. In this case, there are a few possible
215 stacking sequences for the $a/3\langle 111 \rangle$ loops, which are demonstrated in Figure 7. Figure 7(a) shows
216 the perfect stacking. By comparison, Figure 7(b-d) indicate two inserted atomic layers (U and N
217 layer) differently: “S” denotes normal stacking in the sublattice leading to a standard stack fault
218 and “OS” denotes overlapping stacking, which would be prohibited in an FCC structure, but can
219 be stabilized with interweaving atomic layers with an opposite charge. Using the same notation
220 for the insert layers, Figure 8 compares the formation energy of a loop with 3 nm in diameter (the
221 only difference lies in the stacking). Figure 7(d) corresponds to the lowest energy configuration.
222 With this stacking, the stacking fault energy (γ) is calculated to be 1.54 J/m^2 . Also, such stacking
223 is used for the energetic calculations for faulted loops at different sizes. For $a/2\langle 110 \rangle$ loop, the
224 double-layer $\{110\}$ stacking is shown in Figure 9, with each layer containing an equal number of
225 interstitials of both atom types. After identifying the stacking, loops at different radii are created
226 in the shape of disk in the simulation box. Then the system is relaxed during an energy
227 minimization so that the system pressure tensor is reduced to zero; this is followed by multiple
228 rounds of static minimization with conjugate gradient method.

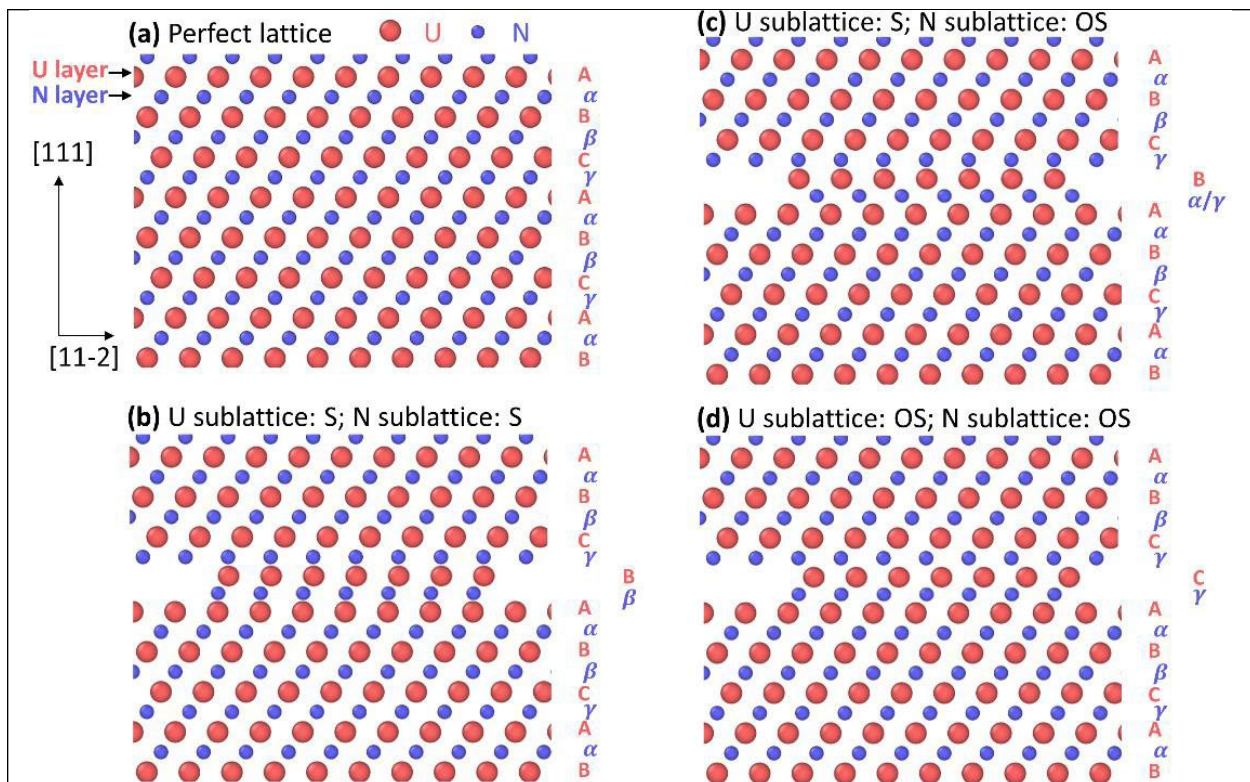


Figure 7. (a) Perfect lattice stacking; (c-d) different stacking for the inserted two layers (U and N layers, shape in disk). S: normal stacking in the sublattice; OS: overlapping stacking in the sublattice.

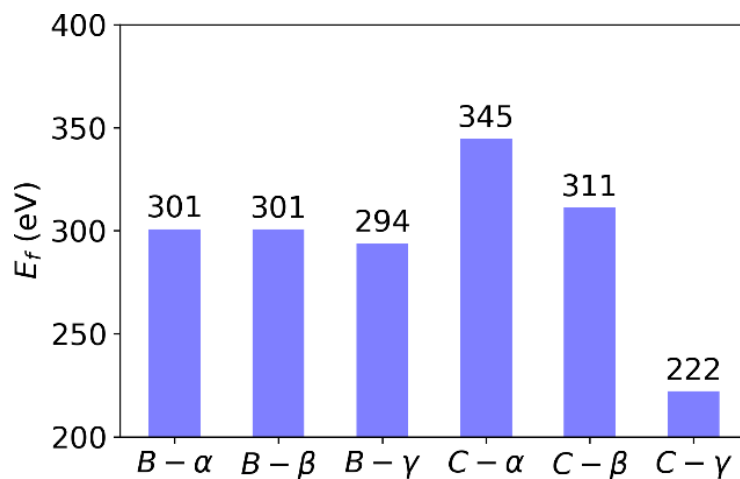
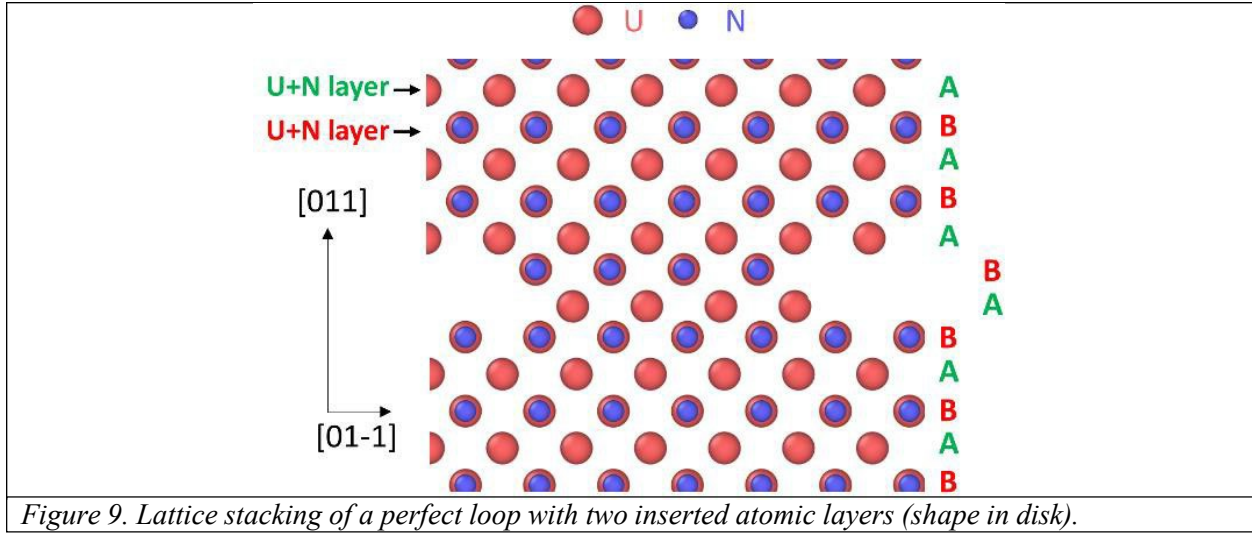


Figure 8. Formation energy of 3.0 nm diameter faulted loops for different stacking. The labels denote the stacking of the two insert atomic layers (see Figure 7b-d). Lowest energy (C- γ) corresponds to Figure 7(d).



The loop formation energies are compared as a function of loop size as shown in Figure 10. It is expected that the faulted loop becomes energetically less favorable as loop size increases, because of the energy penalty from stacking fault [69]. As the loop size is below ~ 6 nm in diameter, $a/3\langle 111 \rangle$ extrinsic loop is slightly energetically favorable, while as the size becomes larger, there is an energetic preference to transform to a perfect loop. This can be achieved by nucleating Shockley partial dislocations [70] to initiate the unfaulting process. Note that due to the energy barrier of dislocation nucleation and migration [70], one may observe large faulted loops, especially at low temperatures without deformation. In other words, a distribution of faulted loop size around the critical size still exists due to kinetics. Although the average dislocation loop size is 6.2 ± 1.7 nm at 400°C [9], which is close to the critical size of ~ 6 nm calculated by MS simulation, $a/3\langle 111 \rangle$ faulted loops were not observed in this work. The observation indicates the unfaulting process of dislocation loops in irradiated UN might happen at even smaller size. A similar unfaulting process has been observed in neutron [71] and proton [67] irradiated ZrC, where ZrC shares the same crystal structure as UN. Faulted dislocation loops formed with the average size of 4.3 ± 0.5 nm and 5.8 ± 0.6 nm in proton irradiated ZrC up to 0.7 dpa and 1.5 dpa,

respectively, at 800°C [67], while only unfaulted perfect dislocation loops with the average size of 9.85 nm were observed in proton irradiated ZrC up to 2 dpa at 1125°C [72]. Therefore, to reveal the unfaulting process in UN, proton irradiation experiment at lower temperature, i.e. <400°C, or lower dose, needs to be pursued in future studies.

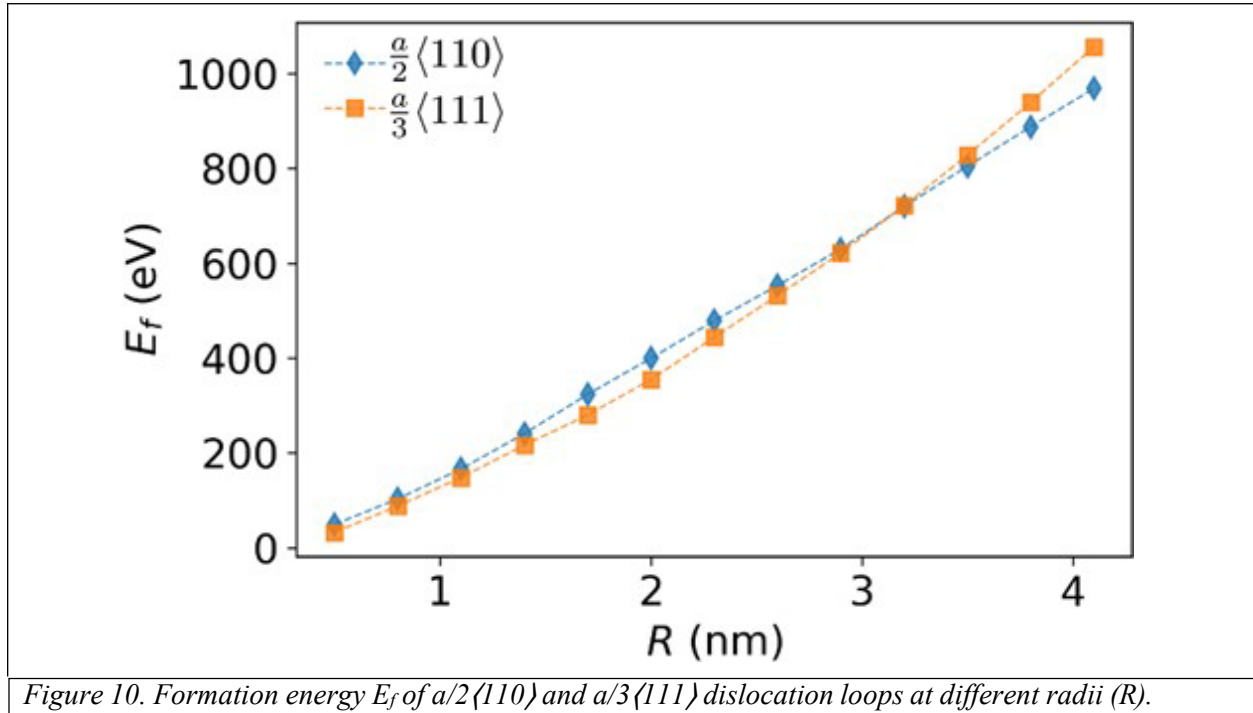


Figure 10. Formation energy E_f of $a/2\langle 110 \rangle$ and $a/3\langle 111 \rangle$ dislocation loops at different radii (R).

In this study, only $a/2\langle 111 \rangle$ type of dislocation loops formed after proton irradiation at two temperatures in α - U_2N_3 that has a Mn_2O_3 -type BCC crystal structure. It has been extensively reported in BCC-based ferritic alloys that perfect $a/2\langle 111 \rangle$ and $a\langle 100 \rangle$ loops can form under irradiation [73–81]. It would have been interesting to compare the formation energy of these two types of dislocation loops in α - U_2N_3 using MS calculation, but the interatomic potential of α - U_2N_3 has not been developed. Similar $a/2\langle 111 \rangle$ perfect dislocation loop formation was observed in In_2O_3 [82] that has the same Mn_2O_3 -type BCC crystal structure, where these loops formed from misfitting inclusions at smaller misfit values than straight dislocations during In_2O_3 nanorod

growth rather than under irradiation. To fully understand the defect evolution under irradiation in α - U_2N_3 , the loop formation mechanism needs to be further explored via well-designed experiments and modeling.

The dislocation loop type in proton irradiated UO_2 is in good agreement with that in proton irradiated ThO_2 , where only $a/3\langle 111 \rangle$ faulted dislocation loops were found [40]. The average loop size is quite small of 3.3 nm [9] and 4.5 nm [40] in proton irradiated UO_2 and ThO_2 , respectively. On the contrary, only $a/2\langle 110 \rangle$ perfect loops of larger size were observed in heavy ion irradiated UO_2 [23–25] and ThO_2 [41]. Similar to UN, MD calculations of loop formation energy in UO_2 [27,28] and ThO_2 [41] indicate that, $a/3\langle 111 \rangle$ faulted dislocation loops are energetically favorable when their size is less than a few nanometers, above which the unfaulting process may occur.

Irradiation induced defects may affect mechanical and thermal properties of ceramic nuclear fuels and their non-radioactive surrogate, cerium dioxide (CeO_2) [16,52,83–87]. The thermal transport behavior in CeO_2 is significantly affected by the type of dislocation loops, where perfect loops only slightly reduce the thermal conductivity while faulted loops lead to an unusually large reduction of thermal conductivity [16]. This was ascribed to extensive phonon scattering because of a stronger strain field surrounding faulted loops. The effects of loop type and size on thermal conductivity may also exist in UN, and more efforts on this topic are needed in the future.

5. Conclusion

The dislocation loop type analysis in proton irradiated UN and α - U_2N_3 phases at 400°C and 710°C, as well as irradiated UO_2 at 710°C are systematically investigated. It is revealed that a single dislocation loop type of $a/2\langle 110 \rangle$, $a/2\langle 111 \rangle$ and $a/3\langle 111 \rangle$ exists in UN, α - U_2N_3 and UO_2 phases, respectively. For the UN phase, MS simulation reveals that the formation energy of

a/3 $\langle 111 \rangle$ faulted loops is lower than a/2 $\langle 110 \rangle$ perfect loops when the dislocation loop size is smaller than 6 nm, which is well below the resolution limit of the selected STEM imaging condition; it explains why only perfect type of dislocation loops are observed in UN at two test temperatures. This result is the first to report the single dislocation loop type formed in the proton irradiated uranium nitrides and uranium dioxide phases, though future work concerning different radiation conditions may be conducted to further investigate other potential dislocation loop type formation in the systems.

Acknowledgements

The microstructural characterization was supported by the U.S. Department of Energy, Office of Nuclear Energy under DOE Idaho Operations Office Contract DEAC07-05ID14517 as part of Nuclear Science User Facilities. The MD/MS simulation was supported by the Center for Thermal Energy Transport under Irradiation (TETI), an Energy Frontier Research Center funded by the U.S. Department of Energy (DOE), Office of Science, Basic Energy Sciences (BES). The synthesis and ion irradiation of UN-UO₂ samples were supported by the U.S. Department of Energy, Office of Nuclear Energy under a Nuclear Energy University Program (award number: DE-NE00120690).

References

- [1] M. Streit, F. Ingold, Nitrides as a nuclear fuel option, *J. Eur. Ceram. Soc.* 25 (2005) 2687–2692. <https://doi.org/10.1016/j.jeurceramsoc.2005.03.181>.
- [2] V.M. Troyanov, A.F. Grachev, L.M. Zabud’ko, M. V. Skupov, Prospects for Using Nitride Fuel in Fast Reactors with a Closed Nuclear Fuel Cycle, *At. Energy.* 117 (2014) 85–91. <https://doi.org/10.1007/s10512-014-9893-1>.
- [3] C. Ekberg, D. Ribeiro Costa, M. Hedberg, M. Jolkkonen, Nitride fuel for Gen IV nuclear

- power systems, *J. Radioanal. Nucl. Chem.* 318 (2018) 1713–1725.
<https://doi.org/10.1007/s10967-018-6316-0>.
- [4] J.P. Gorton, B.S. Collins, A.T. Nelson, N.R. Brown, Reactor performance and safety characteristics of ThN-UN fuel concepts in a PWR, *Nucl. Eng. Des.* 355 (2019) 110317.
<https://doi.org/10.1016/j.nucengdes.2019.110317>.
- [5] D.J. Allen, S.R. Blair, M.G. Millett, M.E. Nelson, Evaluation of Non-Oxide Fuel for Fission-Based Nuclear Reactors on Spacecraft, *Nucl. Technol.* 205 (2019) 755–765.
<https://doi.org/10.1080/00295450.2018.1524228>.
- [6] J.T. White, A.W. Travis, J.T. Dunwoody, A.T. Nelson, Fabrication and thermophysical property characterization of UN/U₃Si₂ composite fuel forms, *J. Nucl. Mater.* 495 (2017) 463–474. <https://doi.org/10.1016/j.jnucmat.2017.08.041>.
- [7] K.A. Terrani, B.C. Jolly, J.M. Harp, Uranium nitride tristructural-isotropic fuel particle, *J. Nucl. Mater.* 531 (2020) 152034. <https://doi.org/10.1016/j.jnucmat.2020.152034>.
- [8] L.G. Gonzalez Fonseca, M. Hedberg, L. Huan, P. Olsson, T. Retegan Vollmer, Application of SPS in the fabrication of UN and (U,Th)N pellets from microspheres, *J. Nucl. Mater.* 536 (2020) 152181. <https://doi.org/10.1016/j.jnucmat.2020.152181>.
- [9] L. He, M. Khafizov, C. Jiang, B. Tyburska-Püschel, B.J. Jaques, P. Xiu, P. Xu, M.K. Meyer, K. Sridharan, D.P. Butt, J. Gan, Phase and defect evolution in uranium-nitrogen-oxygen system under irradiation, *Acta Mater.* 208 (2021) 116778.
<https://doi.org/10.1016/j.actamat.2021.116778>.
- [10] A. Gonzales, J.K. Watkins, A.R. Wagner, B.J. Jaques, E.S. Sooby, Challenges and opportunities to alloyed and composite fuel architectures to mitigate high uranium density fuel oxidation: uranium silicide, *J. Nucl. Mater.* (2021) 153026.
<https://doi.org/10.1016/j.jnucmat.2021.153026>.
- [11] J. Bugl, A. Bauer, Corrosion and oxidation characteristics of uranium mononitride, *Met. Soc., Am. Inst. Mining, Met. Pet. Engrs., Inst. Met. Div., Spec. Rept.* (1964).
- [12] R.M. Dell, V.J. Wheeler, E.J. McIver, Oxidation of uranium mononitride and uranium monocarbide, *Trans. Faraday Soc.* 62 (1966) 3591. <https://doi.org/10.1039/tf9666203591>.
- [13] K. Johnson, V. Ström, J. Wallenius, D.A. Lopes, Oxidation of accident tolerant fuel candidates, *J. Nucl. Sci. Technol.* (2016) 1–7.
<https://doi.org/10.1080/00223131.2016.1262297>.
- [14] J.K. Watkins, A. Gonzales, A.R. Wagner, E.S. Sooby, B.J. Jaques, Challenges and opportunities to alloyed and composite fuel architectures to mitigate high uranium density fuel oxidation: Uranium mononitride, *J. Nucl. Mater.* 553 (2021) 153048.
<https://doi.org/10.1016/j.jnucmat.2021.153048>.
- [15] D.R. Costa, M. Hedberg, S.C. Middleburgh, J. Wallenius, P. Olsson, D.A. Lopes, Oxidation of UN/U₂N₃-UO₂ composites: an evaluation of UO₂ as an oxidation barrier for the nitride phases, *J. Nucl. Mater.* 544 (2021) 152700.
<https://doi.org/10.1016/j.jnucmat.2020.152700>.

- [16] M. Khafizov, J. Pakarinen, L. He, D.H. Hurley, Impact of irradiation induced dislocation loops on thermal conductivity in ceramics, *J. Am. Ceram. Soc.* 102 (2019) 7533–7542. <https://doi.org/10.1111/jace.16616>.
- [17] P.E. Evans, T.J. Davies, Uranium nitrides, *J. Nucl. Mater.* (1963). [https://doi.org/10.1016/0022-3115\(63\)90115-6](https://doi.org/10.1016/0022-3115(63)90115-6).
- [18] B.T.M. Willis, Structures of UO_2 , UO_{2+x} and U_4O_9 by neutron diffraction, *J. Phys.* 25 (1964). <https://doi.org/10.1051/jphys:01964002505043100>.
- [19] Y. Yang, C.A. Dickerson, T.R. Allen, Radiation stability of ZrN under 2.6 MeV proton irradiation, *J. Nucl. Mater.* 392 (2009) 200–205. <https://doi.org/10.1016/j.jnucmat.2009.03.040>.
- [20] L. Jiao, K.Y. Yu, D. Chen, C. Jacob, L. Shao, X. Zhang, H. Wang, Radiation tolerant nanocrystalline ZrN films under high dose heavy-ion irradiations, *J. Appl. Phys.* 117 (2015) 145901. <https://doi.org/10.1063/1.4917381>.
- [21] W. Bao, S. Robertson, J.-X. Liu, G.-J. Zhang, F. Xu, H. Wu, Structural integrity and characteristics at lattice and nanometre levels of ZrN polycrystalline irradiated by 4 MeV Au ions, *J. Eur. Ceram. Soc.* 38 (2018) 4373–4383. <https://doi.org/10.1016/j.jeurceramsoc.2018.05.013>.
- [22] A.D. Whapham, B.E. Sheldon, Radiation damage in uranium dioxide, *Philos. Mag.* 12 (1965) 1179–1192. <https://doi.org/10.1080/14786436508228669>.
- [23] L.F. He, M. Gupta, C.A. Yablinsky, J. Gan, M.A. Kirk, X.M. Bai, J. Pakarinen, T.R. Allen, In situ TEM observation of dislocation evolution in Kr-irradiated UO_2 single crystal, *J. Nucl. Mater.* (2013). <https://doi.org/10.1016/j.jnucmat.2013.06.050>.
- [24] C. Onofri, C. Sabathier, C. Baumier, C. Bachelet, H. Palancher, M. Legros, Evolution of extended defects in polycrystalline Au-irradiated UO_2 using in situ TEM: Temperature and fluence effects, *J. Nucl. Mater.* (2016). <https://doi.org/10.1016/j.jnucmat.2016.10.011>.
- [25] C. Onofri, M. Legros, J. L  chelle, H. Palancher, C. Baumier, C. Bachelet, C. Sabathier, Full characterization of dislocations in ion-irradiated polycrystalline UO_2 , *J. Nucl. Mater.* (2017). <https://doi.org/10.1016/j.jnucmat.2017.07.043>.
- [26] J. Soullard, Mise en evidence de boucles de dislocation imparfaites dans des echantillons de bioxyde d’uranium irradies, *J. Nucl. Mater.* 78 (1978) 125–130. [https://doi.org/10.1016/0022-3115\(78\)90511-1](https://doi.org/10.1016/0022-3115(78)90511-1).
- [27] A. Le Prioux, P. Fossati, S. Maillard, T. Jourdan, P. Maugis, Empirical potential simulations of interstitial dislocation loops in uranium dioxide, *J. Nucl. Mater.* 479 (2016) 576–584. <https://doi.org/10.1016/j.jnucmat.2016.07.046>.
- [28] A. Chartier, C. Onofri, L. Van Brutzel, C. Sabathier, O. Dorosh, J. Jagielski, Early stages of irradiation induced dislocations in urania, *Appl. Phys. Lett.* 109 (2016) 181902. <https://doi.org/10.1063/1.4967191>.
- [29] X.-Y. Liu, D.A. Andersson, Small uranium and oxygen interstitial clusters in UO_2 : An empirical potential study, *J. Nucl. Mater.* 547 (2021) 152783.

<https://doi.org/10.1016/j.jnucmat.2021.152783>.

- [30] C. Lu, T. Yang, K. Jin, N. Gao, P. Xiu, Y. Zhang, F. Gao, H. Bei, W.J. Weber, K. Sun, Y. Dong, L. Wang, Radiation-induced segregation on defect clusters in single-phase concentrated solid-solution alloys, *Acta Mater.* 127 (2017) 98–107. <https://doi.org/10.1016/j.actamat.2017.01.019>.
- [31] L. Zhang, C. Lu, G. Michal, G. Deng, K. Tieu, The formation and destruction of stacking fault tetrahedron in fcc metals: A molecular dynamics study, *Scr. Mater.* 136 (2017) 78–82. <https://doi.org/10.1016/j.scriptamat.2017.04.019>.
- [32] C. Lu, T. Yang, L. Niu, Q. Peng, K. Jin, M.L. Crespillo, G. Velisa, H. Xue, F. Zhang, P. Xiu, Y. Zhang, F. Gao, H. Bei, W.J. Weber, L. Wang, Interstitial migration behavior and defect evolution in ion irradiated pure nickel and Ni-xFe binary alloys, *J. Nucl. Mater.* 509 (2018) 237–244. <https://doi.org/10.1016/j.jnucmat.2018.07.006>.
- [33] C.J. Ulmer, A.T. Motta, Characterization of faulted dislocation loops and cavities in ion irradiated alloy 800H, *J. Nucl. Mater.* 498 (2018) 458–467. <https://doi.org/10.1016/j.jnucmat.2017.11.012>.
- [34] T. Yang, C. Lu, G. Velisa, K. Jin, P. Xiu, M.L. Crespillo, Y. Zhang, H. Bei, L. Wang, Effect of alloying elements on defect evolution in Ni-20X binary alloys, *Acta Mater.* 151 (2018) 159–168. <https://doi.org/10.1016/j.actamat.2018.03.054>.
- [35] P. Xiu, Y.N. Osetsky, L. Jiang, G. Velisa, Y. Tong, H. Bei, W.J. Weber, Y. Zhang, L. Wang, Dislocation loop evolution and radiation hardening in nickel-based concentrated solid solution alloys, *J. Nucl. Mater.* 538 (2020) 152247. <https://doi.org/10.1016/j.jnucmat.2020.152247>.
- [36] D. Chen, K. Murakami, K. Dohi, K. Nishida, Z. Li, N. Sekimura, The effects of loop size on the unfauling of Frank loops in heavy ion irradiation, *J. Nucl. Mater.* 529 (2020) 151942. <https://doi.org/10.1016/j.jnucmat.2019.151942>.
- [37] T. Chen, L. He, M.H. Cullison, C. Hay, J. Burns, Y. Wu, L. Tan, The correlation between microstructure and nanoindentation property of neutron-irradiated austenitic alloy D9, *Acta Mater.* 195 (2020) 433–445. <https://doi.org/10.1016/j.actamat.2020.05.020>.
- [38] C. Chen, J. Zhang, J. Song, Comprehensive study of vacancy frank loop unfauling: atomistic simulations and predictive model, *Acta Mater.* 208 (2021) 116745. <https://doi.org/10.1016/j.actamat.2021.116745>.
- [39] D.L. DOUGLASS, S.E. BRONISZ, Alpha Particle Irradiation Damage in ThO₂, *J. Am. Ceram. Soc.* 54 (1971) 158–161. <https://doi.org/10.1111/j.1151-2916.1971.tb12245.x>.
- [40] K. Bawane, X. Liu, T. Yao, M. Khafizov, A. French, J.M. Mann, L. Shao, J. Gan, D.H. Hurley, L. He, TEM characterization of dislocation loops in proton irradiated single crystal ThO₂, *J. Nucl. Mater.* 552 (2021) 152998. <https://doi.org/10.1016/j.jnucmat.2021.152998>.
- [41] L. He, T. Yao, K. Bawane, M. Jin, C. Jiang, M. Khafizov, X. Liu, W.-Y. Chen, J.M. Mann, D.H. Hurley, J. Gan, Dislocation loop evolution in Kr-irradiated ThO₂, *J. Am. Ceram. Soc.* submitted (2021).

- [42] B. Yao, D.J. Edwards, R.J. Kurtz, TEM characterization of dislocation loops in irradiated bcc Fe-based steels, *J. Nucl. Mater.* (2013). <https://doi.org/10.1016/j.jnucmat.2012.12.002>.
- [43] C.M. Parish, K.G. Field, A.G. Certain, J.P. Wharry, Application of STEM characterization for investigating radiation effects in BCC Fe-based alloys, *J. Mater. Res.* (2015). <https://doi.org/10.1557/jmr.2015.32>.
- [44] P. Xiu, H. Bei, Y. Zhang, L. Wang, K.G. Field, STEM Characterization of Dislocation Loops in Irradiated FCC Alloys, *J. Nucl. Mater.* (2021). <https://doi.org/10.1016/j.jnucmat.2020.152658>.
- [45] K.G. Field, S.A. Briggs, X. Hu, Y. Yamamoto, R.H. Howard, K. Sridharan, Heterogeneous dislocation loop formation near grain boundaries in a neutron-irradiated commercial FeCrAl alloy, *J. Nucl. Mater.* (2017). <https://doi.org/10.1016/j.jnucmat.2016.10.050>.
- [46] K.G. Field, S.A. Briggs, K. Sridharan, Y. Yamamoto, R.H. Howard, Dislocation loop formation in model FeCrAl alloys after neutron irradiation below 1 dpa, *J. Nucl. Mater.* (2017). <https://doi.org/10.1016/j.jnucmat.2017.07.061>.
- [47] Y. Zhang, X. Wang, Y.N. Osetsky, Y. Tong, R. Harrison, S.E. Donnelly, D. Chen, Y. Wang, H. Bei, B.C. Sales, K.L. More, P. Xiu, L. Wang, W.J. Weber, Effects of 3d electron configurations on helium bubble formation and void swelling in concentrated solid-solution alloys, *Acta Mater.* 181 (2019) 519–529. <https://doi.org/10.1016/j.actamat.2019.10.013>.
- [48] Y. Zhu, C. Ophus, M.B. Toloczko, D.J. Edwards, Towards bend-contour-free dislocation imaging via diffraction contrast STEM, *Ultramicroscopy.* (2018). <https://doi.org/10.1016/j.ultramic.2018.06.001>.
- [49] Y. Miyajima, M. Mitsuhashi, S. Hata, H. Nakashima, N. Tsuji, Quantification of internal dislocation density using scanning transmission electron microscopy in ultrafine grained pure aluminium fabricated by severe plastic deformation, *Mater. Sci. Eng. A.* (2010). <https://doi.org/10.1016/j.msea.2010.09.058>.
- [50] P.J. Phillips, M.C. Brandes, M.J. Mills, M. de Graef, Diffraction contrast STEM of dislocations: Imaging and simulations, *Ultramicroscopy.* (2011). <https://doi.org/10.1016/j.ultramic.2011.07.001>.
- [51] C.B. Carter, D.B. Williams, *Transmission electron microscopy: Diffraction, imaging, and spectrometry*, 2016. <https://doi.org/10.1007/978-3-319-26651-0>.
- [52] C.A. Dennett, W.R. Deskins, M. Khafizov, Z. Hua, A. Khanolkar, K. Bawane, L. Fu, J.M. Mann, C.A. Marianetti, L. He, D.H. Hurley, A. El-Azab, An integrated experimental and computational investigation of defect and microstructural effects on thermal transport in thorium dioxide, *Acta Mater.* 213 (2021) 116934. <https://doi.org/10.1016/j.actamat.2021.116934>.
- [53] W.J. Weber, Y. Zhang, Predicting damage production in monoatomic and multi-elemental targets using stopping and range of ions in matter code: Challenges and recommendations, *Curr. Opin. Solid State Mater. Sci.* (2019). <https://doi.org/10.1016/j.cossms.2019.06.001>.

- [54] E.H. Lee, L.K. Mansur, M.H. Yoo, Spatial variation in void volume during charged particle bombardment - the effects of injected interstitials, *J. Nucl. Mater.* (1979). [https://doi.org/10.1016/0022-3115\(79\)90548-8](https://doi.org/10.1016/0022-3115(79)90548-8).
- [55] F.A. Garner, Impact of the injected interstitial on the correlation of charged particle and neutron-induced radiation damage, *J. Nucl. Mater.* (1983). [https://doi.org/10.1016/0022-3115\(83\)90023-5](https://doi.org/10.1016/0022-3115(83)90023-5).
- [56] P.J. Phillips, M.J. Mills, M. De Graef, Systematic row and zone axis STEM defect image simulations, *Philos. Mag.* (2011). <https://doi.org/10.1080/14786435.2010.547526>.
- [57] P. Humble, M.H. Loretto, L.M. Clarebrough, The nature of defects in quenched nickel, *Philos. Mag.* (1967). <https://doi.org/10.1080/14786436708227702>.
- [58] D.J. Mazey, J.A. Hudson, Observation of large faulted interstitial loops in proton-irradiated nickel, *J. Nucl. Mater.* (1970). [https://doi.org/10.1016/0022-3115\(70\)90177-7](https://doi.org/10.1016/0022-3115(70)90177-7).
- [59] H.R. Brager, J.L. Straalsund, Defect development in neutron irradiated type 316 stainless steel, *J. Nucl. Mater.* (1973). [https://doi.org/10.1016/0022-3115\(73\)90131-1](https://doi.org/10.1016/0022-3115(73)90131-1).
- [60] M.J. Whelan, P.B. Hirsch, Electron diffraction from crystals containing stacking faults: II, *Philos. Mag.* (1957). <https://doi.org/10.1080/14786435708243208>.
- [61] M.. Sole, C.. Van Der Walt, Oxidation and deformation studies of uranium nitride by electron microscopy, *Acta Metall.* 16 (1968) 501–510. [https://doi.org/10.1016/0001-6160\(68\)90124-7](https://doi.org/10.1016/0001-6160(68)90124-7).
- [62] S. Plimpton, Fast Parallel Algorithms for Short-Range Molecular Dynamics, *J. Comput. Phys.* 117 (1995) 1–19. <https://doi.org/10.1006/jcph.1995.1039>.
- [63] V.I. Tseplyaev, S.V. Starikov, The atomistic simulation of pressure-induced phase transition in uranium mononitride, *J. Nucl. Mater.* 480 (2016) 7–14. <https://doi.org/10.1016/j.jnucmat.2016.07.048>.
- [64] E.A. Kotomin, R.W. Grimes, Y. Mastrikov, N.J. Ashley, Atomic scale DFT simulations of point defects in uranium nitride, *J. Phys. Condens. Matter.* 19 (2007) 106208. <https://doi.org/10.1088/0953-8984/19/10/106208>.
- [65] C. Dickerson, Y. Yang, T.R. Allen, Defects and microstructural evolution of proton irradiated titanium carbide, *J. Nucl. Mater.* 424 (2012) 62–68. <https://doi.org/10.1016/j.jnucmat.2012.02.005>.
- [66] S. Agarwal, T. Koyanagi, A. Bhattacharya, L. Wang, Y. Katoh, X. Hu, M. Pagan, S.J. Zinkle, Neutron irradiation-induced microstructure damage in ultra-high temperature ceramic TiC, *Acta Mater.* 186 (2020) 1–10. <https://doi.org/10.1016/j.actamat.2019.12.022>.
- [67] Y. Yang, C.A. Dickerson, H. Swoboda, B. Miller, T.R. Allen, Microstructure and mechanical properties of proton irradiated zirconium carbide, *J. Nucl. Mater.* 378 (2008) 341–348. <https://doi.org/10.1016/j.jnucmat.2008.06.042>.
- [68] F. Wang, X. Yan, T. Wang, Y. Wu, L. Shao, M. Nastasi, Y. Lu, B. Cui, Irradiation damage in (Zr_{0.25}Ta_{0.25}Nb_{0.25}Ti_{0.25})C high-entropy carbide ceramics, *Acta Mater.* 195

(2020) 739–749. <https://doi.org/10.1016/j.actamat.2020.06.011>.

[69] J.P. Hirth, J. Lothe, T. Mura, Theory of Dislocations (2nd ed.), J. Appl. Mech. 50 (1983) 476–477. <https://doi.org/10.1115/1.3167075>.

[70] T. Kadoyoshi, H. Kaburaki, F. Shimizu, H. Kimizuka, S. Jitsukawa, J. Li, Molecular dynamics study on the formation of stacking fault tetrahedra and unfaulting of Frank loops in fcc metals, Acta Mater. 55 (2007) 3073–3080. <https://doi.org/10.1016/j.actamat.2007.01.010>.

[71] L.L. Snead, Y. Katoh, S. Kondo, Effects of fast neutron irradiation on zirconium carbide, J. Nucl. Mater. 399 (2010) 200–207. <https://doi.org/10.1016/j.jnucmat.2010.01.020>.

[72] Y. Yang, W.-Y. Lo, C. Dickerson, T.R. Allen, Stoichiometry effect on the irradiation response in the microstructure of zirconium carbides, J. Nucl. Mater. 454 (2014) 130–135. <https://doi.org/10.1016/j.jnucmat.2014.07.071>.

[73] B.L. Eyre, R. Bullough, On the formation of interstitial loops in b.c.c. metals, Philos. Mag. (1965). <https://doi.org/10.1080/14786436508224943>.

[74] J. Marian, B.D. Wirth, J.M. Perlado, Mechanism of Formation and Growth of [Formula presented] Interstitial Loops in Ferritic Materials, Phys. Rev. Lett. (2002). <https://doi.org/10.1103/PhysRevLett.88.255507>.

[75] K. Arakawa, M. Hatanaka, E. Kuramoto, K. Ono, H. Mori, Changes in the burgers vector of perfect dislocation loops without contact with the external dislocations, Phys. Rev. Lett. (2006). <https://doi.org/10.1103/PhysRevLett.96.125506>.

[76] S.L. Dudarev, R. Bullough, P.M. Derlet, Effect of the α - γ Phase transition on the stability of dislocation loops in bcc iron, Phys. Rev. Lett. (2008). <https://doi.org/10.1103/PhysRevLett.100.135503>.

[77] Z. Yao, M.L. Jenkins, M. Hernández-Mayoral, M.A. Kirk, The temperature dependence of heavy-ion damage in iron: A microstructural transition at elevated temperatures, in: Philos. Mag., 2010. <https://doi.org/10.1080/14786430903430981>.

[78] K. Arakawa, T. Amino, H. Mori, Direct observation of the coalescence process between nanoscale dislocation loops with different Burgers vectors, Acta Mater. (2011). <https://doi.org/10.1016/j.actamat.2010.09.018>.

[79] J. Chen, N. Gao, P. Jung, T. Sauvage, A new mechanism of loop formation and transformation in bcc iron without dislocation reaction, J. Nucl. Mater. (2013). <https://doi.org/10.1016/j.jnucmat.2013.05.074>.

[80] H. Xu, R.E. Stoller, Y.N. Osetsky, D. Terentyev, Solving the puzzle of 100 Interstitial Loop Formation in bcc Iron, Phys. Rev. Lett. (2013). <https://doi.org/10.1103/PhysRevLett.110.265503>.

[81] Q. Peng, F. Meng, Y. Yang, C. Lu, H. Deng, L. Wang, S. De, F. Gao, Shockwave generates < 100 > dislocation loops in bcc iron, Nat. Commun. (2018). <https://doi.org/10.1038/s41467-018-07102-3>.

- 541 [82] D. Maestre, D. Häussler, A. Cremades, W. Jäger, J. Piqueras, Complex
Defect Structure in
542 the Core of Sn-Doped In₂O₃ Nanorods and Its Relationship with a
Dislocation-Driven
543 Growth Mechanism, *J. Phys. Chem. C*. 115 (2011) 18083–18087.
544 <https://doi.org/10.1021/jp204579u>.
- 545 [83] J. Pakarinen, M. Khafizov, L. He, C. Wetteland, J. Gan, A.T. Nelson, D.H.
Hurley, A. El-
546 Azab, T.R. Allen, Microstructure changes and thermal conductivity
reduction in UO₂
547 following 3.9 MeV He²⁺ ion irradiation, *J. Nucl. Mater.* 454 (2014) 283–
289.
548 <https://doi.org/10.1016/j.jnucmat.2014.07.053>.
- 549 [84] M.S. Elbakhshwan, Y. Miao, J.F. Stubbins, B.J. Heuser, Mechanical
properties of UO₂
550 thin films under heavy ion irradiation using nanoindentation and finite
element modeling,
551 *J. Nucl. Mater.* 479 (2016) 548–558.
<https://doi.org/10.1016/j.jnucmat.2016.07.047>.
- 552 [85] M. Khafizov, M.F. Riyad, Y. Wang, J. Pakarinen, L. He, T. Yao, A. El-
Azab, D. Hurley,
553 Combining mesoscale thermal transport and x-ray diffraction
measurements to
554 characterize early-stage evolution of irradiation-induced defects in
ceramics, *Acta Mater.*
555 193 (2020) 61–70. <https://doi.org/10.1016/j.actamat.2020.04.018>.
- 556 [86] V.S. Chauhan, J. Pakarinen, T. Yao, L. He, D.H. Hurley, M. Khafizov,
Indirect
557 characterization of point defects in proton irradiated ceria, *Materialia*. 15
(2021) 101019.
558 <https://doi.org/10.1016/j.mtla.2021.101019>.
- 559 [87] C.A. Dennett, Z. Hua, A. Khanolkar, T. Yao, P.K. Morgan, T.A. Prusnick,
N. Poudel, A.
560 French, K. Gofryk, L. He, L. Shao, M. Khafizov, D.B. Turner, J.M. Mann,
D.H. Hurley,
561 The influence of lattice defects, recombination, and clustering on thermal
transport in
562 single crystal thorium dioxide, *APL Mater.* 8 (2020) 111103.
563 <https://doi.org/10.1063/5.0025384>.